

Resonances in axially symmetric dielectric objects

Johan Helsing* and Anders Karlsson†

December 9, 2024

Abstract

A high-order convergent and robust numerical solver is constructed and used to find complex eigenwavenumbers and electromagnetic eigenfields of dielectric objects with axial symmetry. The solver is based on Fourier–Nyström discretization of Müller’s combined integral equations for the transmission problem and can be applied to demanding resonance problems at microwave, terahertz, and optical wavelengths. High achievable accuracy, even at very high wavenumbers, makes the solver ideal for benchmarking and for assessing the performance of general purpose commercial software.

1 Introduction

When a dielectric object in vacuum is excited by an electromagnetic pulse, it emits electromagnetic waves also after the pulse has passed the object. These waves, emitted without an external source, are due to resonances whose frequencies and attenuation constants are determined by the material and shape of the object. This paper is about the fundamental problem of determining such resonances of axially symmetric homogeneous dielectric objects in vacuum. The problem is formulated as an eigenvalue problem based on a combination of the electric and magnetic field integral equations, (EFIE) and (MFIE), and two charge integral equation (ChIEs). It is solved numerically using a high-order convergent discretization scheme.

Resonances in dielectric objects are common in nature and technology. Already at ultra-low frequencies the earth exhibits Schumann resonances, which are electromagnetic waves, excited by lightning, that are confined to the region between the ground and the ionosphere [17, Ch. 8.9]. Most antennas are designed to have a resonance at the frequency of operation. By combining an antenna with a dielectric resonator, the size of the antenna can be reduced [19] due to the shorter wavelength in the dielectric material. A similar concept is used for the design of narrow-band dielectric band-pass

*Centre for Mathematical Sciences, Lund University, Sweden

†Electrical and Information Technology, Lund University, Sweden

and band-stop microwave filters [24]. Resonant structures play an important role in the recent progress in nano-optics. A good example is axially symmetric structures that exhibit whispering gallery modes (WGMs) [21]. The WGMs have large Q-factors (commercial micro-optical WGM resonators can have $Q > 10^8$) and their eigenfields are confined to a small volume in the outer part of the dielectric object. These properties are very useful in the design of microcavity lasers [11] and extremely sensitive sensors [7] and for the generation of frequency combs [4, 18].

Common numerical methods for the determination of electromagnetic resonances in dielectric objects include the finite element method (FEM) [23], boundary integral equation (BIE) methods [3, 14, 15], the discrete dipole approximation (DDA) method [1], and the null-field method [31]. The method used in the present paper belongs to the category of BIE methods, which comprise a variety of formulations and techniques. We rely on the Müller integral equations [22, Section 23] and a modification of the Fourier–Nyström scheme of [15], which in turn draws on progress in [5, 12, 13, 14, 30].

Most BIE methods for transmission problems use the electric and magnetic surface current densities as unknowns. A particular feature of the present work is that we also let the surface charge densities be unknowns. There are two reasons for this: First, the problem of evaluating compact differences of hypersingular operators in the classical Müller formulation is avoided. Second, numerical differentiation of surface currents for the evaluation of eigenfields is avoided. As a result, our scheme can be made higher-order and attain extraordinary accuracy. It can easily solve resonance problems that, to our knowledge, previously have been essentially inaccessible.

We remark that the use of unknown surface charge densities to improve the performance of numerical schemes is not new. It was introduced as a way to overcome the, so called, low frequency breakdown problem of BIE methods in [26] and was further developed for this purpose in [27]. In [14] and [15] it was recognized that the use of unknown surface charges is numerically favorable also at higher frequencies.

The paper is organized as follows: Section 2 is on geometry. Section 3 formulates our problem in terms of partial differential equations (PDEs). Section 4 introduces integral representations of electric and magnetic fields in terms of surface densities and derives and discusses our version of the Müller integral equations. Section 5 restricts the analysis to axially symmetric objects. Fourier series expansions are used to express the homogeneous system of integral equations, from which wavenumbers and surface densities representing eigenfields are obtained, in a form that is well-suited for discretization. Section 6 defines useful physical quantities and relate them to the surface densities. The numerical method is described in Section 7. Some challenging numerical examples, involving various types of resonant modes, are given in Section 8.

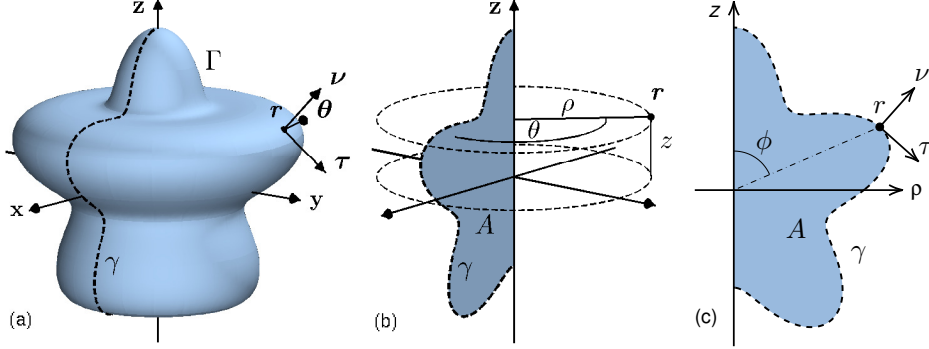


Figure 1: An axisymmetric surface Γ generated by a curve γ . (a) A point \mathbf{r} on Γ has outward unit normal $\boldsymbol{\nu}$ and tangential vectors $\boldsymbol{\tau}$ and $\boldsymbol{\theta}$. (b) \mathbf{r} has radial distance ρ , azimuthal angle θ , and height z . The planar domain A is bounded by γ and the z -axis. (c) Coordinate axes and vectors in the half-plane $\theta = 0$.

2 Geometry and unit vectors

Let Γ be an axially symmetric surface enclosing a three-dimensional domain V_2 (a body of revolution). The domain outside $V_2 \cup \Gamma$ is unbounded and denoted V_1 . Let

$$\mathbf{r} = \hat{\mathbf{r}}|\mathbf{r}| = (x, y, z) = (\rho \cos \theta, \rho \sin \theta, z) \quad (1)$$

denote a point in \mathbb{R}^3 . Here $\rho = \sqrt{x^2 + y^2}$ is the distance from the z -axis, θ is the azimuthal angle, and $\hat{\mathbf{r}}$ is the radial unit vector. The outward unit normal $\boldsymbol{\nu}$ at a point \mathbf{r} on Γ is

$$\boldsymbol{\nu} = (\nu_\rho \cos \theta, \nu_\rho \sin \theta, \nu_z). \quad (2)$$

We also use the unit vectors

$$\begin{aligned} \boldsymbol{\rho} &= (\cos \theta, \sin \theta, 0), \\ \boldsymbol{\theta} &= (-\sin \theta, \cos \theta, 0), \\ \boldsymbol{\tau} &= \boldsymbol{\theta} \times \boldsymbol{\nu} = (\nu_z \cos \theta, \nu_z \sin \theta, -\nu_\rho), \\ \mathbf{z} &= (0, 0, 1), \end{aligned} \quad (3)$$

where $\boldsymbol{\theta}$ and $\boldsymbol{\tau}$ are tangential unit vectors. See Figure 1(a) and 1(b).

The angle $\theta = 0$ defines a half-plane in \mathbb{R}^3 whose intersection with Γ corresponds to a generating curve γ . Let $r = (\rho, z)$ be a point in this half-plane and let A be the planar domain bounded by γ and the z -axis. The outward unit normal on γ is $\boldsymbol{\nu} = (\nu_\rho, \nu_z)$ and $\boldsymbol{\tau} = (\nu_z, -\nu_\rho)$ is a tangent. See Figure 1(c).

3 Problem formulation

The domain V_2 is a homogeneous dielectric object with constant complex refractive index m . In V_1 there is vacuum. The electric field is everywhere scaled with the free space wave impedance η_0 such that $\mathbf{E}(\mathbf{r}) = \eta_0^{-1} \mathbf{E}'(\mathbf{r})$, where $\mathbf{E}'(\mathbf{r})$ is the unscaled field. Then \mathbf{E} and the magnetic field \mathbf{H} have the same dimensions.

Sources can be located in a bounded volume V_{s1} in V_1 and V_{s2} in V_2 and generate time harmonic incident fields with complex electric and magnetic fields $\mathbf{E}_1^{\text{inc}}, \mathbf{H}_1^{\text{inc}}$ in V_1 and $\mathbf{E}_2^{\text{inc}}, \mathbf{H}_2^{\text{inc}}$ in V_2 . These give rise to the scattered fields \mathbf{E}^{sca} and \mathbf{H}^{sca} in V_1 and V_2 . We prefer to work with the total electric and magnetic fields \mathbf{E} and \mathbf{H} , which are the sum of the incident and scattered fields. From the Maxwell equations it follows that the total fields satisfy the system of PDEs

$$\nabla^2 \mathbf{E}(\mathbf{r}) + k_j^2 \mathbf{E}(\mathbf{r}) = \mathbf{0}, \quad \mathbf{r} \in V_j \setminus V_{sj}, \quad j = 1, 2, \quad (4)$$

$$\nabla^2 \mathbf{H}(\mathbf{r}) + k_j^2 \mathbf{H}(\mathbf{r}) = \mathbf{0}, \quad \mathbf{r} \in V_j \setminus V_{sj}, \quad j = 1, 2, \quad (5)$$

$$\nabla \cdot \mathbf{E}(\mathbf{r}) = 0, \quad \mathbf{r} \in V_j \setminus V_{sj}, \quad j = 1, 2, \quad (6)$$

$$\nabla \cdot \mathbf{H}(\mathbf{r}) = 0, \quad \mathbf{r} \in V_j \setminus V_{sj}, \quad j = 1, 2, \quad (7)$$

$$k_2 = mk_1, \quad (8)$$

where $k_1 = \omega/c$ and k_2 are the wavenumbers in V_1 and V_2 , ω is the angular frequency, and c is the speed of light in vacuum. We use the time dependence $e^{-i\omega t}$. Then $\Im\{m\} > 0$, since the material in V_2 is assumed to be passive. From now on, we omit the subscript of k_1 and write the (vacuum) wavenumber in V_1 as k .

The boundary conditions on Γ are

$$\lim_{V_1 \ni \mathbf{r} \rightarrow \mathbf{r}^\circ} \boldsymbol{\nu}^\circ \times \mathbf{E}(\mathbf{r}) = \lim_{V_2 \ni \mathbf{r} \rightarrow \mathbf{r}^\circ} \boldsymbol{\nu}^\circ \times \mathbf{E}(\mathbf{r}), \quad \mathbf{r}^\circ \in \Gamma, \quad (9)$$

$$\lim_{V_1 \ni \mathbf{r} \rightarrow \mathbf{r}^\circ} \boldsymbol{\nu}^\circ \times \mathbf{H}(\mathbf{r}) = \lim_{V_2 \ni \mathbf{r} \rightarrow \mathbf{r}^\circ} \boldsymbol{\nu}^\circ \times \mathbf{H}(\mathbf{r}), \quad \mathbf{r}^\circ \in \Gamma, \quad (10)$$

$$\lim_{V_1 \ni \mathbf{r} \rightarrow \mathbf{r}^\circ} \boldsymbol{\nu}^\circ \cdot \mathbf{E}(\mathbf{r}) = \lim_{V_2 \ni \mathbf{r} \rightarrow \mathbf{r}^\circ} m^2 \boldsymbol{\nu}^\circ \cdot \mathbf{E}(\mathbf{r}), \quad \mathbf{r}^\circ \in \Gamma, \quad (11)$$

$$\lim_{V_1 \ni \mathbf{r} \rightarrow \mathbf{r}^\circ} \boldsymbol{\nu}^\circ \cdot \mathbf{H}(\mathbf{r}) = \lim_{V_2 \ni \mathbf{r} \rightarrow \mathbf{r}^\circ} \boldsymbol{\nu}^\circ \cdot \mathbf{H}(\mathbf{r}), \quad \mathbf{r}^\circ \in \Gamma, \quad (12)$$

and the radiation condition for the scattered field in V_1 is

$$\begin{aligned} \mathbf{E}^{\text{sca}}(\mathbf{r}) &= \frac{e^{ik|\mathbf{r}|}}{|\mathbf{r}|} \left(\mathbf{F}(\hat{\mathbf{r}}) + \mathcal{O}\left(\frac{1}{|\mathbf{r}|}\right) \right), \quad |\mathbf{r}| \rightarrow \infty, \\ \mathbf{H}^{\text{sca}}(\mathbf{r}) &= \frac{e^{ik|\mathbf{r}|}}{|\mathbf{r}|} \left(\hat{\mathbf{r}} \times \mathbf{F}(\hat{\mathbf{r}}) + \mathcal{O}\left(\frac{1}{|\mathbf{r}|}\right) \right), \quad |\mathbf{r}| \rightarrow \infty, \end{aligned} \quad (13)$$

where \mathbf{F} is the electric far-field pattern, see [6, Eq. (6.23)].

Our resonance problem can now be formulated as follows: we seek non-trivial solutions to (4)-(13) when the incident fields are zero. The solutions are the eigenwavenumbers k and the eigenfields \mathbf{E} and \mathbf{H} .

3.1 The radiation condition at complex wavenumbers

We shall solve (4)-(13) using a BIE method where the integral equations are derived from integral representations of \mathbf{E} and \mathbf{H} containing the Green's function

$$\Phi_k(\mathbf{r}, \mathbf{r}') = \frac{e^{ik|\mathbf{r}-\mathbf{r}'|}}{4\pi|\mathbf{r}-\mathbf{r}'|}. \quad (14)$$

The radiation condition (13) is then automatically satisfied and says that, for real k and in the far zone, the scattered field is an outward traveling spherical vector wave.

At resonances, the eigenwavenumbers k are complex with negative imaginary part. The condition (13) then says that the eigenfields grow exponentially at large distances. This is required for the fields to satisfy causality and for the corresponding time domain fields to be exponentially decaying as $e^{\Im\{k\}ct}$ in time. Causality says that the fields of a resonance at a time t and at a distance $|\mathbf{r}|$ from an object left the object at time $t - |\mathbf{r}|/c$. The attenuation implies that at time $t - |\mathbf{r}|/c$, the fields in the object were $e^{-\Im\{k\}r}$ times stronger than at time t , in accordance with (13).

The condition (13) is vital in the derivation of integral representations of \mathbf{E} and \mathbf{H} in V_1 . In [28, Section IIC] it is shown that such derivations hold also for eigenfields with complex eigenwavenumbers, despite their exponential growth in the radial direction.

4 Integral representations and integral equations

This section gives integral representations of \mathbf{E} and \mathbf{H} along with our system of BIEs for a general three-dimensional dielectric object. The integral representations use four fictitious surface densities on Γ : the magnetic and electric surface current densities \mathbf{M}_s and \mathbf{J}_s , and the electric and magnetic surface charge densities ϱ_E and ϱ_M . The system of BIEs contain the EFIE, the MFIE, the electric ChIE (EChIE), and the magnetic ChIE (MChIE). It is based on the combination introduced by Müller in [22, Section 23].

4.1 Surface densities

The densities \mathbf{M}_s , \mathbf{J}_s , ϱ_E , and ϱ_M are defined from a viewpoint in V_1 :

$$\mathbf{M}_s(\mathbf{r}^\circ) \equiv \lim_{V_1 \ni \mathbf{r} \rightarrow \mathbf{r}^\circ} \mathbf{E}(\mathbf{r}) \times \boldsymbol{\nu}^\circ = \lim_{V_2 \ni \mathbf{r} \rightarrow \mathbf{r}^\circ} \mathbf{E}(\mathbf{r}) \times \boldsymbol{\nu}^\circ, \quad \mathbf{r}^\circ \in \Gamma, \quad (15)$$

$$\mathbf{J}_s(\mathbf{r}^\circ) \equiv \lim_{V_1 \ni \mathbf{r} \rightarrow \mathbf{r}^\circ} \boldsymbol{\nu}^\circ \times \mathbf{H}(\mathbf{r}) = \lim_{V_2 \ni \mathbf{r} \rightarrow \mathbf{r}^\circ} \boldsymbol{\nu}^\circ \times \mathbf{H}(\mathbf{r}), \quad \mathbf{r}^\circ \in \Gamma, \quad (16)$$

$$\varrho_E(\mathbf{r}^\circ) \equiv \lim_{V_1 \ni \mathbf{r} \rightarrow \mathbf{r}^\circ} \boldsymbol{\nu}^\circ \cdot \mathbf{E}(\mathbf{r}) = \lim_{V_2 \ni \mathbf{r} \rightarrow \mathbf{r}^\circ} m^2 \boldsymbol{\nu}^\circ \cdot \mathbf{E}(\mathbf{r}), \quad \mathbf{r}^\circ \in \Gamma, \quad (17)$$

$$\varrho_M(\mathbf{r}^\circ) \equiv \lim_{V_1 \ni \mathbf{r} \rightarrow \mathbf{r}^\circ} \boldsymbol{\nu}^\circ \cdot \mathbf{H}(\mathbf{r}) = \lim_{V_2 \ni \mathbf{r} \rightarrow \mathbf{r}^\circ} \boldsymbol{\nu}^\circ \cdot \mathbf{H}(\mathbf{r}), \quad \mathbf{r}^\circ \in \Gamma. \quad (18)$$

The second equalities in (15)-(18) hold when the boundary conditions (9)-(12) are met.

4.2 Integral representations

Our integral representations of $\mathbf{E}(\mathbf{r})$ and $\mathbf{H}(\mathbf{r})$ are for $\mathbf{r} \in V_1$

$$\begin{aligned}\mathbf{E}(\mathbf{r}) &= \mathbf{E}_1^{\text{inc}}(\mathbf{r}) - \mathcal{N}_{\varrho_E}(\mathbf{r}) - \mathcal{K}\mathbf{M}_s(\mathbf{r}) + ik\mathcal{S}\mathbf{J}_s(\mathbf{r}), \\ \mathbf{H}(\mathbf{r}) &= \mathbf{H}_1^{\text{inc}}(\mathbf{r}) + ik\mathcal{S}\mathbf{M}_s(\mathbf{r}) + \mathcal{K}\mathbf{J}_s(\mathbf{r}) - \mathcal{N}_{\varrho_M}(\mathbf{r}),\end{aligned}\tag{19}$$

and for $\mathbf{r} \in V_2$

$$\begin{aligned}\mathbf{E}(\mathbf{r}) &= \mathbf{E}_2^{\text{inc}}(\mathbf{r}) + m^{-2}\tilde{\mathcal{N}}_{\varrho_E}(\mathbf{r}) + \tilde{\mathcal{K}}\mathbf{M}_s(\mathbf{r}) - ik\tilde{\mathcal{S}}\mathbf{J}_s(\mathbf{r}), \\ \mathbf{H}(\mathbf{r}) &= \mathbf{H}_2^{\text{inc}}(\mathbf{r}) - im^2k\tilde{\mathcal{S}}\mathbf{M}_s(\mathbf{r}) - \tilde{\mathcal{K}}\mathbf{J}_s(\mathbf{r}) + \tilde{\mathcal{N}}_{\varrho_M}(\mathbf{r}),\end{aligned}\tag{20}$$

where the integral operators \mathcal{S} , \mathcal{N} , and \mathcal{K} are defined by their actions on scalar or vector surface densities $g(\mathbf{r})$ and $\mathbf{g}(\mathbf{r})$ as

$$\mathcal{S}g(\mathbf{r}) = \int_{\Gamma} \Phi_k(\mathbf{r}, \mathbf{r}')g(\mathbf{r}') d\Gamma',\tag{21}$$

$$\mathcal{N}g(\mathbf{r}) = \int_{\Gamma} \nabla \Phi_k(\mathbf{r}, \mathbf{r}')g(\mathbf{r}') d\Gamma',\tag{22}$$

$$\mathcal{K}\mathbf{g}(\mathbf{r}) = \int_{\Gamma} \nabla \Phi_k(\mathbf{r}, \mathbf{r}') \times \mathbf{g}(\mathbf{r}') d\Gamma',\tag{23}$$

and $\tilde{\mathcal{S}}$, $\tilde{\mathcal{N}}$, and $\tilde{\mathcal{K}}$ are defined analogously, but with Φ_k replaced by Φ_{k_2} .

4.3 Integral equations

Our BIEs on Γ come from using (19) and (20) in the definitions (15)-(18) and taking the limits $\mathbf{r} \rightarrow \mathbf{r}^\circ \in \Gamma$. Each definition gives rise to two BIEs: one for $\mathbf{r} \in V_1$ and one for $\mathbf{r} \in V_2$.

The BIEs coming from $\mathbf{r} \in V_1$ are

$$\begin{aligned}\varrho_E + 2\boldsymbol{\nu} \cdot (\mathcal{N}_{\varrho_E} + \mathcal{K}\mathbf{M}_s - ik\mathcal{S}\mathbf{J}_s) &= 2\boldsymbol{\nu} \cdot \mathbf{E}_1^{\text{inc}}, \\ \mathbf{M}_s - 2\boldsymbol{\nu} \times (\mathcal{N}_{\varrho_E} + \mathcal{K}\mathbf{M}_s - ik\mathcal{S}\mathbf{J}_s) &= -2\boldsymbol{\nu} \times \mathbf{E}_1^{\text{inc}}, \\ \mathbf{J}_s - 2\boldsymbol{\nu} \times (ik\mathcal{S}\mathbf{M}_s + \mathcal{K}\mathbf{J}_s - \mathcal{N}_{\varrho_M}) &= 2\boldsymbol{\nu} \times \mathbf{H}_1^{\text{inc}}, \\ \varrho_M - 2\boldsymbol{\nu} \cdot (ik\mathcal{S}\mathbf{M}_s + \mathcal{K}\mathbf{J}_s - \mathcal{N}_{\varrho_M}) &= 2\boldsymbol{\nu} \cdot \mathbf{H}_1^{\text{inc}}.\end{aligned}\tag{24}$$

The BIEs coming from $\mathbf{r} \in V_2$ are

$$\begin{aligned}\varrho_E - 2\boldsymbol{\nu} \cdot (\tilde{\mathcal{N}}_{\varrho_E} + m^2\tilde{\mathcal{K}}\mathbf{M}_s - im^2k\tilde{\mathcal{S}}\mathbf{J}_s) &= 2m^2\boldsymbol{\nu} \cdot \mathbf{E}_2^{\text{inc}}, \\ \mathbf{M}_s + 2\boldsymbol{\nu} \times (m^{-2}\tilde{\mathcal{N}}_{\varrho_E} + \tilde{\mathcal{K}}\mathbf{M}_s - ik\tilde{\mathcal{S}}\mathbf{J}_s) &= -2\boldsymbol{\nu} \times \mathbf{E}_2^{\text{inc}}, \\ \mathbf{J}_s + 2\boldsymbol{\nu} \times (im^2k\tilde{\mathcal{S}}\mathbf{M}_s + \tilde{\mathcal{K}}\mathbf{J}_s - \tilde{\mathcal{N}}_{\varrho_M}) &= 2\boldsymbol{\nu} \times \mathbf{H}_2^{\text{inc}}, \\ \varrho_M + 2\boldsymbol{\nu} \cdot (im^2k\tilde{\mathcal{S}}\mathbf{M}_s + \tilde{\mathcal{K}}\mathbf{J}_s - \tilde{\mathcal{N}}_{\varrho_M}) &= 2\boldsymbol{\nu} \cdot \mathbf{H}_2^{\text{inc}}.\end{aligned}\tag{25}$$

The order of the equations in (24) and (25) is from top to bottom: EChIE, EFIE, MFIE, and MChIE.

We collect the systems (24) and (25) in block operator form

$$\mathbf{Q}_1 \boldsymbol{\sigma} = \mathbf{f}_1, \quad (26)$$

$$\mathbf{Q}_2 \boldsymbol{\sigma} = \mathbf{f}_2, \quad (27)$$

where

$$\boldsymbol{\sigma} = \begin{bmatrix} \varrho_E \\ \mathbf{M}_s \\ \mathbf{J}_s \\ \varrho_M \end{bmatrix}, \quad \mathbf{f}_1 = 2 \begin{bmatrix} \boldsymbol{\nu} \cdot \mathbf{E}_1^{\text{inc}} \\ -\boldsymbol{\nu} \times \mathbf{E}_1^{\text{inc}} \\ \boldsymbol{\nu} \times \mathbf{H}_1^{\text{inc}} \\ \boldsymbol{\nu} \cdot \mathbf{H}_1^{\text{inc}} \end{bmatrix}, \quad \mathbf{f}_2 = 2 \begin{bmatrix} m^2 \boldsymbol{\nu} \cdot \mathbf{E}_2^{\text{inc}} \\ -\boldsymbol{\nu} \times \mathbf{E}_2^{\text{inc}} \\ \boldsymbol{\nu} \times \mathbf{H}_2^{\text{inc}} \\ \boldsymbol{\nu} \cdot \mathbf{H}_2^{\text{inc}} \end{bmatrix}, \quad (28)$$

and where \mathbf{Q}_1 and \mathbf{Q}_2 are square block operator matrices. The system (26) is, modulo normalization constants, identical to [26, Eq. 18]. Our resonance problem means that we must find simultaneous nontrivial solutions to (26) and (27) when $\mathbf{f}_1 = \mathbf{f}_2 = \mathbf{0}$.

4.4 The ChIE-extended Müller formulation

Müller suggested that (26) and (27) be combined into

$$(\mathbf{Q}_1 + \mathbf{Q}_2) \boldsymbol{\sigma} = \mathbf{f}_1 + \mathbf{f}_2, \quad (29)$$

and we follow that suggestion.

There are, however, some differences between (29) and Müller's original combined system. Müller adopted a technique that is often applied to the MFIE and the EFIE, where the surface charge densities are replaced by the surface current densities according to

$$\varrho_E(\mathbf{r}) = -\frac{i}{k} \nabla_s \cdot \mathbf{J}_s(\mathbf{r}), \quad (30)$$

$$\varrho_M(\mathbf{r}) = -\frac{i}{k} \nabla_s \cdot \mathbf{M}_s(\mathbf{r}), \quad (31)$$

and where $\nabla_s \cdot (\)$ is the surface divergence. The divergence is then moved to the kernels by integration by parts. The resulting integral equations are by that only expressed in terms of \mathbf{M}_s and \mathbf{J}_s , but some of the integral operators involved become hypersingular. Fortunately, these hypersingularities cancel out in the sum $\mathbf{Q}_1 + \mathbf{Q}_2$ and one can prove that Müller's version of (29) is a system of Fredholm second kind integral equations with compact integral operators [22, p. 300]. In contrast, our versions of \mathbf{Q}_1 and \mathbf{Q}_2 are free from hypersingular integral operators but they do contain singular operators defined only in the sense of the Cauchy principal value and do not all cancel out in the sum $\mathbf{Q}_1 + \mathbf{Q}_2$. In accordance with [29], we refer to Müller's

version of (29) as the classical Müller formulation. The present (29) we call the ChIE-extended Müller formulation.

Müller showed two additional properties of his classical formulation under the condition that Γ consists of only one closed regular surface:

1. The system (29) has a unique solution $\boldsymbol{\sigma}$ for wavenumbers k with $0 \leq \arg\{k\} < \pi$, [22, Theorem 68].
2. With $\boldsymbol{\sigma}$ as the unique solution to (29), the corresponding fields \boldsymbol{E} and \boldsymbol{H} obtained from (19) and (20) are solutions to the Maxwell equations [22, Theorem 69]. By that they also satisfy (4)-(13).

Without presenting a proof, we assume that the ChIE-extended Müller formulation (29) also has these properties. Furthermore, in our numerical experiments with $\boldsymbol{f}_1 = \boldsymbol{f}_2 = \mathbf{0}$ we check that all nontrivial solutions to (29) also solve (26) and (27) to the same precision and that (30) and (31) hold (with a few digits lost in the numerical differentiation). We have not been able to detect any solution to (29) that violates these tests.

4.5 Physical resonances

Our goal is to find eigenwavenumbers k for the homogeneous version of (29)

$$(\mathbf{Q}_1 + \mathbf{Q}_2)\boldsymbol{\sigma} = \mathbf{0} \quad (32)$$

and to evaluate their corresponding eigenfields \boldsymbol{E} and \boldsymbol{H} from (19) and (20) via $\boldsymbol{\sigma}$. The eigenwavenumbers have $\Im\{k\} < 0$ and constitute an infinite countable set.

It is important that the system (32) gives all physical nontrivial solutions to (4)-(13) and no spurious solutions. We now argue that this is the case. As assumed in Section 4.4, the system (29) has a unique solution for all k with $0 \leq \arg\{k\} < \pi$. Now consider an incident electromagnetic wave $\boldsymbol{E}_1^{\text{inc}}(\boldsymbol{r}, t)$ in the time domain that has compact support in time at \boldsymbol{r} so that, after a certain time, the incident field has passed V_2 . We Fourier transform the incident wave in time to get \boldsymbol{f}_1 in (29) for all real k . For each k , the unique solution $\boldsymbol{\sigma}$ is then obtained from (29) and the unique time domain fields are obtained from (19) and (20) by an inverse Fourier transform. An alternative is to use the singular expansion method (SEM) [16] which is based on the method of contour integration. For large enough times, the inverse Fourier transform is evaluated by closing the integration path along the real k -axis by a half circle in the lower half plane and use of the residue theorem. The expressions for the time domain fields contain sums of the residue contributions from all SEM poles in the lower half plane. The complex wavenumbers of the SEM poles are the eigenwavenumbers of (32). The time domain fields obtained from these two alternative methods must be the same and the sum of pole contributions is by that unique.

Since this reasoning is valid for a large class of incident waves, the set of eigenwavenumbers of (32) contains all physical, but no spurious, resonances.

We remark that spurious resonances for dielectric objects is a problem for many commercial software packages. If these resonances cannot be eliminated by the software, then the delicate task to separate them from the physical resonances is left to the user.

5 Axial symmetry

So far our analysis is valid for arbitrary dielectric objects. We now restrict it to objects with axial symmetry and perform an azimuthal Fourier transformation of (26) and (27) and of (19) and (20) to obtain modal integral equations and modal representations of \mathbf{E} and \mathbf{H} . The fields \mathbf{E} and \mathbf{H} are expressed in the cylindrical coordinates (ρ, θ, z) as

$$\begin{aligned}\mathbf{E}(\mathbf{r}) &= \rho E_\rho(\mathbf{r}) + \theta E_\theta(\mathbf{r}) + z E_z(\mathbf{r}), \\ \mathbf{H}(\mathbf{r}) &= \rho H_\rho(\mathbf{r}) + \theta H_\theta(\mathbf{r}) + z H_z(\mathbf{r}).\end{aligned}\tag{33}$$

The densities \mathbf{M}_s and \mathbf{J}_s are decomposed in the two tangential directions $\boldsymbol{\tau}$ and $\boldsymbol{\theta}$, see Figure 1, as

$$\begin{aligned}\mathbf{M}_s(\mathbf{r}) &= \boldsymbol{\tau} M_\tau(\mathbf{r}) + \boldsymbol{\theta} M_\theta(\mathbf{r}), \\ \mathbf{J}_s(\mathbf{r}) &= \boldsymbol{\tau} J_\tau(\mathbf{r}) + \boldsymbol{\theta} J_\theta(\mathbf{r}).\end{aligned}\tag{34}$$

5.1 Fourier series expansions

Let $g(\mathbf{r})$ represent a surface density or a right hand side and let G represent an integral operator of Section 4.2 or 4.3 with rotationally invariant kernel $G(\mathbf{r}, \mathbf{r}')$. The azimuthal Fourier coefficients $g_n(r)$ and $G_n(r, r')$ of the functions $g(\mathbf{r})$ and $G(\mathbf{r}, \mathbf{r}')$ are

$$g_n(r) = \frac{1}{\sqrt{2\pi}} \int_{-\pi}^{\pi} e^{-in\theta} g(\mathbf{r}) d\theta,\tag{35}$$

$$G_n(r, r') = \frac{1}{\sqrt{2\pi}} \int_{-\pi}^{\pi} e^{-in(\theta-\theta')} G(\mathbf{r}, \mathbf{r}') d(\theta - \theta').\tag{36}$$

The subscript n is the azimuthal index, $n = 0, \pm 1, \pm 2, \dots$. We also define modal integral operators G_n in terms of the coefficients $G_n(r, r')$ as

$$G_n g_n(r) = \sqrt{2\pi} \int_{\gamma} G_n(r, r') g_n(r') \rho' d\gamma'.\tag{37}$$

The singularities of $G(\mathbf{r}, \mathbf{r}')$ are inherited by $G_n(r, r')$ in the sense that weakly singular operators G on Γ correspond to weakly singular operators G_n on γ , and that the same holds for Cauchy-type singular operators.

5.2 Modal integral equations

Using (34) and with the notation (35), the Fourier coefficients of the vectors in (28) each gets six scalar entries (transformed scalar surface densities)

$$\boldsymbol{\sigma}_n = \begin{bmatrix} \varrho E_n \\ M_{\tau n} \\ M_{\theta n} \\ J_{\tau n} \\ J_{\theta n} \\ \varrho M_n \end{bmatrix}, \quad \mathbf{f}_{1n} = 2 \begin{bmatrix} E_{1\nu n}^{\text{inc}} \\ E_{1\theta n}^{\text{inc}} \\ -E_{1\tau n}^{\text{inc}} \\ -H_{1\theta n}^{\text{inc}} \\ H_{1\tau n}^{\text{inc}} \\ H_{1\nu n}^{\text{inc}} \end{bmatrix}, \quad \mathbf{f}_{2n} = 2 \begin{bmatrix} m^2 E_{2\nu n}^{\text{inc}} \\ E_{2\theta n}^{\text{inc}} \\ -E_{2\tau n}^{\text{inc}} \\ -H_{2\theta n}^{\text{inc}} \\ H_{2\tau n}^{\text{inc}} \\ H_{2\nu n}^{\text{inc}} \end{bmatrix}. \quad (38)$$

The modal counterpart of (26) and (27) becomes

$$\mathbf{Q}_{1n} \boldsymbol{\sigma}_n = \mathbf{f}_{1n}, \quad (39)$$

$$\mathbf{Q}_{2n} \boldsymbol{\sigma}_n = \mathbf{f}_{2n}. \quad (40)$$

The block operator matrices \mathbf{Q}_{1n} and \mathbf{Q}_{2n} can be written

$$\mathbf{Q}_{1n} = \begin{bmatrix} I + 2K_{\nu n} & -2iK_{25n} & 2K_{26n} & -2ikS_{5n} & 2kS_{6n} & 0 \\ -2iK_{12n} & I - K_{1n} & -iK_{2n} & 2kS_{3n} & -2ikS_{4n} & 0 \\ 2K_{24n} & -iK_{3n} & I - K_{4n} & 2ikS_{1n} & -2kS_{2n} & 0 \\ 0 & -2kS_{3n} & 2ikS_{4n} & I - K_{1n} & -iK_{2n} & 2iK_{12n} \\ 0 & -2ikS_{1n} & 2kS_{2n} & -iK_{3n} & I - K_{4n} & -2K_{24n} \\ 0 & -2ikS_{5n} & 2kS_{6n} & 2iK_{25n} & -2K_{26n} & I + 2K_{\nu n} \end{bmatrix}, \quad (41)$$

and

$$\mathbf{Q}_{2n} = \begin{bmatrix} I - 2\tilde{K}_{\nu n} & 2im^2\tilde{K}_{25n} & -2m^2\tilde{K}_{26n} & 2im^2k\tilde{S}_{5n} & -2m^2k\tilde{S}_{6n} & 0 \\ 2im^{-2}\tilde{K}_{12n} & I + \tilde{K}_{1n} & i\tilde{K}_{2n} & -2k\tilde{S}_{3n} & 2ik\tilde{S}_{4n} & 0 \\ -2m^{-2}\tilde{K}_{24n} & i\tilde{K}_{3n} & I + \tilde{K}_{4n} & -2ik\tilde{S}_{1n} & 2k\tilde{S}_{2n} & 0 \\ 0 & 2m^2k\tilde{S}_{3n} & -2im^2k\tilde{S}_{4n} & I + \tilde{K}_{1n} & i\tilde{K}_{2n} & -2i\tilde{K}_{12n} \\ 0 & 2im^2k\tilde{S}_{1n} & -2m^2k\tilde{S}_{2n} & i\tilde{K}_{3n} & I + \tilde{K}_{4n} & 2\tilde{K}_{24n} \\ 0 & 2im^2k\tilde{S}_{5n} & -2m^2k\tilde{S}_{6n} & -2i\tilde{K}_{25n} & 2\tilde{K}_{26n} & I - 2\tilde{K}_{\nu n} \end{bmatrix}, \quad (42)$$

where I is the identity, S_{in} and K_{in} , with various indices i , are modal operators stemming from \mathcal{S} , \mathcal{N} , and \mathcal{K} and generally defined via (36) and (37), and the tilde symbol means the replacement of k by k_2 as explained in Section 4.2. The operators S_{in} are weakly singular. The K_{in} are weakly singular for $i = \nu, 1, 2, 3, 4$ and Cauchy-type singular for $i = 12, 24, 25, 26$.

All modal operators in (41) and (42) are detailed in [15, Appendix A] except for K_{in} , $i = 24, 25, 26$, which are given in Appendix A of the present paper.

5.3 Modal representations of E and H

Once the modal counterpart of (29),

$$(\mathbf{Q}_{1n} + \mathbf{Q}_{2n}) \boldsymbol{\sigma}_n = \mathbf{f}_{1n} + \mathbf{f}_{2n}, \quad (43)$$

has been solved for $\boldsymbol{\sigma}_n$, modal representations of \mathbf{E} and \mathbf{H} can be constructed from modal counterparts of (19) and (20).

The modal representations of the fields in V_1 are

$$\begin{aligned} E_{\rho n}(r) &= K_{11n} \varrho_{En} - iK_{5n} M_{\tau n} - K_{6n} M_{\theta n} + ikS_{7n} J_{\tau n} + kS_{8n} J_{\theta n}, \\ E_{\theta n}(r) &= iK_{12n} \varrho_{En} - K_{7n} M_{\tau n} - iK_{8n} M_{\theta n} + kS_{9n} J_{\tau n} + ikS_{10n} J_{\theta n}, \\ E_{zn}(r) &= K_{13n} \varrho_{En} - iK_{9n} M_{\tau n} - K_{10n} M_{\theta n} + ikS_{11n} J_{\tau n}, \end{aligned} \quad (44)$$

and

$$\begin{aligned} H_{\rho n}(r) &= ikS_{7n} M_{\tau n} + kS_{8n} M_{\theta n} + iK_{5n} J_{\tau n} + K_{6n} J_{\theta n} + K_{11n} \varrho_{Mn}, \\ H_{\theta n}(r) &= kS_{9n} M_{\tau n} + ikS_{10n} M_{\theta n} + K_{7n} J_{\tau n} + iK_{8n} J_{\theta n} + iK_{12n} \varrho_{Mn}, \\ H_{zn}(r) &= ikS_{11n} M_{\tau n} + iK_{9n} J_{\tau n} + K_{10n} J_{\theta n} + K_{13n} \varrho_{Mn}. \end{aligned} \quad (45)$$

The modal representations of the fields in V_2 are

$$\begin{aligned} E_{\rho n}(r) &= -m^{-2} \tilde{K}_{11n} \varrho_{En} + i\tilde{K}_{5n} M_{\tau n} + \tilde{K}_{6n} M_{\theta n} - ik\tilde{S}_{7n} J_{\tau n} - k\tilde{S}_{8n} J_{\theta n}, \\ E_{\theta n}(r) &= -im^{-2} \tilde{K}_{12n} \varrho_{En} + \tilde{K}_{7n} M_{\tau n} + i\tilde{K}_{8n} M_{\theta n} - k\tilde{S}_{9n} J_{\tau n} - ik\tilde{S}_{10n} J_{\theta n}, \\ E_{zn}(r) &= -m^{-2} \tilde{K}_{13n} \varrho_{En} + i\tilde{K}_{9n} M_{\tau n} + \tilde{K}_{10n} M_{\theta n} - ik\tilde{S}_{11n} J_{\tau n}, \end{aligned} \quad (46)$$

and

$$\begin{aligned} H_{\rho n}(r) &= -im^2 k\tilde{S}_{7n} M_{\tau n} - m^2 k\tilde{S}_{8n} M_{\theta n} - i\tilde{K}_{5n} J_{\tau n} - \tilde{K}_{6n} J_{\theta n} - \tilde{K}_{11n} \varrho_{Mn}, \\ H_{\theta n}(r) &= -m^2 k\tilde{S}_{9n} M_{\tau n} - im^2 k\tilde{S}_{10n} M_{\theta n} - \tilde{K}_{7n} J_{\tau n} - i\tilde{K}_{8n} J_{\theta n} - i\tilde{K}_{12n} \varrho_{Mn}, \\ H_{zn}(r) &= -im^2 k\tilde{S}_{11n} M_{\tau n} - i\tilde{K}_{9n} J_{\tau n} - \tilde{K}_{10n} J_{\theta n} - \tilde{K}_{13n} \varrho_{Mn}. \end{aligned} \quad (47)$$

Here the operators S_{in} and K_{in} , with various indices i , are detailed in [14] and [15, Appendix A].

5.4 Eigenwavenumbers, eigenfields, and fundamental modes

The eigenwavenumbers at a prescribed refractive index m are wavenumbers k for which, for some azimuthal index n , there exist nontrivial solutions $\boldsymbol{\sigma}_n$ to the homogeneous version of (43)

$$(\mathbf{Q}_{1n} + \mathbf{Q}_{2n}) \boldsymbol{\sigma}_n = \mathbf{0}. \quad (48)$$

Our resonance problem now means finding such numbers k , corresponding eigendensities $\boldsymbol{\sigma}_n$, and eigenfields $\mathbf{E}_n(\mathbf{r})$, $\mathbf{H}_n(\mathbf{r})$ represented by (44)-(47).

In [15] it was shown how to form the physical time-domain fields $\mathbf{E}_n(\mathbf{r}, t)$ from the Fourier coefficient vector $\mathbf{E}_n(r)$. It was shown that one can let $E_{\rho n}(r) = E_{\rho(-n)}(r)$. Then the physical component $E_{\rho n}(\mathbf{r}, t)$ becomes

$$E_{\rho n}(\mathbf{r}, t) = \frac{1}{2} \Re\{(E_{\rho n}(r)e^{in\theta} + E_{\rho(-n)}(r)e^{-in\theta})e^{i\omega t}\}. \quad (49)$$

Since $\omega = kc$, we get

$$\omega \equiv \omega_r - i\alpha = \Re\{k\}c + i\Im\{k\}c, \quad (50)$$

where ω_r is the real angular frequency and α is the attenuation constant. Then

$$E_{\rho n}(\mathbf{r}, t) = \Re\{E_{\rho n}(r)e^{i\omega_r t}\} \cos n\theta e^{-\alpha t}. \quad (51)$$

This is a standing wave in the azimuthal direction. Also $E_{zn}(\mathbf{r}, t)$ and $H_{\theta n}(\mathbf{r}, t)$ are proportional to $\cos n\theta$ whereas $E_{\theta n}(\mathbf{r}, t)$, $H_{\rho n}(\mathbf{r}, t)$, and $H_{zn}(\mathbf{r}, t)$ are proportional to $\sin n\theta$. If one lets $E_{\rho n}(r) = -E_{\rho(-n)}(r)$, then $\cos n\theta$ and $\sin n\theta$ are exchanged in all components.

It is convenient to introduce the concept of the fundamental mode. The fundamental mode, for a given n , is the resonance with the smallest value of $|\Re\{k\}|$. For large n , it has properties that distinguishes it from other resonances: Its electric and magnetic fields are confined to a small volume in V_2 and are strongly attenuated in the proximity of that small volume. The exponential growth of the fields, in concordance with (13), is only seen at large distances. The ratio ω_r/α is large. Fundamental modes with large n are WGMs and are important in optical applications as described in Section 1.

6 Powers, energies, and far-fields

The resonance problem is a non-self-adjoint problem. By that, there is no inner product under which the eigenfields are orthogonal. It is also impossible to uniquely define a stored energy, a radiated power of an eigenfield, and a normalization. It is, nevertheless, relevant to introduce approximate expressions for these quantities and to define the related Q-factor. We define the stored energy as the electromagnetic energy stored in V_2 and define the radiated power as the power radiated from Γ . The sharpness, or quality, of these definitions becomes better as $|\Re\{k\}|/|\Im\{k\}|$ increases.

Assume a single resonance with azimuthal index n that is excited by an incident field for $t < 0$ and that there are no incident fields for $t \geq 0$. According to (51), the physical eigenfield then oscillates with the angular frequency ω_r and attenuates as $e^{-\alpha t}$ for $t \geq 0$. For $t \geq 0$ we let $P_{\text{rad}}(t)$ denote the radiated power through Γ averaged over one period $[t, t + T]$, $P_{\text{diss}}(t)$ the dissipated power averaged over the same period, and $W(t)$ the stored electromagnetic energy in V_2 at time t . Conservation of energy and (51) lead to the relations

$$P(t) = P_{\text{rad}}(t) + P_{\text{diss}}(t), \quad (52)$$

$$P_{\text{rad}}(t) = P_{\text{rad}}(0)e^{-2\alpha t}, \quad (53)$$

$$P_{\text{diss}}(t) = P_{\text{diss}}(0)e^{-2\alpha t}, \quad (54)$$

$$W(t) = W(0)e^{-2\alpha t}, \quad (55)$$

$$W(0) \equiv \int_0^\infty P(t) dt = \frac{P_{\text{rad}}(0) + P_{\text{diss}}(0)}{2\alpha}. \quad (56)$$

We use the standard definition of the Q-factor which, with (50), can be written

$$Q \equiv \omega_r \frac{W(t)}{P(t)} = -\frac{\Re\{k\}}{2\Im\{k\}}, \quad (57)$$

and introduce

$$Q_{\text{rad}} = \omega_r \frac{W(t)}{P_{\text{rad}}(t)}, \quad (58)$$

$$Q_{\text{diss}} = \omega_r \frac{W(t)}{P_{\text{diss}}(t)}, \quad (59)$$

so that, from (52) and (57),

$$\frac{1}{Q} = \frac{1}{Q_{\text{rad}}} + \frac{1}{Q_{\text{diss}}}. \quad (60)$$

The radiated power from V_2 equals the real part of the Poynting vector integrated over Γ

$$\begin{aligned} P_{\text{rad}}(t) &= \frac{1}{2} \Re \left\{ \int_{\gamma} \nu \cdot (\mathbf{E}_n(r) \times \mathbf{H}_n^*(r)) \rho d\gamma \right\} e^{-2\alpha t}, \\ &= \frac{1}{2} \Re \left\{ \int_{\gamma} (M_{\theta n}(r) J_{\tau n}^*(r) - M_{\tau n}(r) J_{\theta n}^*(r)) \rho d\gamma \right\} e^{-2\alpha t}. \end{aligned} \quad (61)$$

From Gauss theorem and the Maxwell equations it also follows that

$$P_{\text{rad}}(0) = -P_{\text{diss}}(0) - \Im\{k\} \int_A (|\mathbf{H}_n(r)|^2 + \Re\{m^2\} |\mathbf{E}_n(r)|^2) \rho dA, \quad (62)$$

and due to (56),

$$W(0) = \frac{1}{2c} \int_A (|\mathbf{H}_n(r)|^2 + \Re\{m^2\} |\mathbf{E}_n(r)|^2) \rho dA. \quad (63)$$

Apart from a scale factor η_0 , see Section 3, the expression (63) is the standard expression for the electromagnetic energy in a volume.

The skin depth

$$\delta = (\Im\{m\} \Re\{k\})^{-1} \quad (64)$$

is a measure of $\Im\{m\}$. It is derived from the attenuation of a plane wave that impinges at normal incidence on a lossy half space, but is also a measure of the attenuation of waves in dielectric objects. When

$$\delta \gg \text{diam}(V_2), \quad (65)$$

a number of approximations are valid: The electric and magnetic eigenfields inside V_2 and on Γ are, to a high degree, independent of $\Im\{m\}$. It then follows, from (61) and (63), that Q_{rad} is independent of $\Im\{m\}$. It also holds that

$$Q_{\text{diss}} \approx \frac{\Re\{m\}}{2\Im\{m\}}. \quad (66)$$

6.1 Far-field pattern

The normalized far-field pattern of a mode with azimuthal index n is

$$\frac{|\mathbf{F}_n(\phi)|}{\max_{0 \leq \phi \leq \pi} |\mathbf{F}_n(\phi)|}, \quad (67)$$

where $\mathbf{F}_n(\phi)$ is the Fourier coefficient of \mathbf{F} in (13), and by that

$$\mathbf{F}_n(\phi) = \lim_{|r| \rightarrow \infty} e^{-ik|r|} |r| \mathbf{E}_n(r). \quad (68)$$

The far-field pattern tells us in what directions the stored energy in V_2 is radiated. By reciprocity it also indicates what direction an incident wave should have in order to excite a resonance. Far-field patterns are included in the numerical examples of Section 8.

7 Discretization

Our Fourier–Nyström discretization scheme for (48) is similar to the scheme used in [15]. This section gives a brief overview and describes some modifications that are appropriate when solving (48) at high wavenumbers.

7.1 Overview

Let G_n be a generic modal integral operator of the type encountered in (48) and let $G_n(r, r')$ and $G(\mathbf{r}, \mathbf{r}')$ be related to G_n as in Section 5.1. We split $G_n(r, r')$ into a smooth and a non-smooth function

$$G_n(r, r') = G_n^{(s)}(r, r') + G_n^{(ns)}(r, r'), \quad (69)$$

where $G_n^{(s)}(r, r')$ is zero when r and r' lie close to each other and $G_n^{(ns)}(r, r')$ is zero otherwise. We also split $G(\mathbf{r}, \mathbf{r}')$ analogously. The kernel split (69) corresponds to an operator split $G_n = G_n^{(s)} + G_n^{(ns)}$.

The discretization of a G_n in (37) results in a square matrix whose entries are values of $G_n(r, r')$, obtained from $G(\mathbf{r}, \mathbf{r}')$ via (36), multiplied with suitable quadrature weights. As underlying quadrature rules we use the trapezoidal rule in (36) and 16th-order panel-based Gauss–Legendre quadrature in (37). This is sufficient for the accurate discretization of the $G_n^{(s)}$.

The efficient discretization of a $G_n^{(ns)}$ requires that a number of techniques are activated, all of which are described in detail in [13, 14, 15]. The most important are: evaluation of the integral over $G^{(ns)}(\mathbf{r}, \mathbf{r}')$ in (36) via factorization and convolution; use of fast discrete Fourier transform techniques and half-integer degree Legendre functions of the second kind [10]

$$\mathfrak{Q}_{n-\frac{1}{2}}(\chi) = \int_{-\pi}^{\pi} \frac{\cos(nt) dt}{\sqrt{8(\chi - \cos(t))}}, \quad (70)$$

with

$$\chi = 1 + \frac{|r - r'|^2}{2\rho\rho'}, \quad (71)$$

to evaluate the Fourier coefficients needed in this convolution; 16th-order accurate product integration for singular integrals on γ , constructed on-the-fly and based on known asymptotics of $\mathfrak{Q}_{n-\frac{1}{2}}(\chi)$ as $\chi \rightarrow 1^+$; a strategy for when to use forward or backward recursion for the evaluation of $\mathfrak{Q}_{n-\frac{1}{2}}(\chi)$; temporary mesh refinement (upsampling) coupled with temporary increase of the quadrature order on γ .

The discretization of the modal representation of \mathbf{E} and \mathbf{H} for $r \notin \gamma$ in Section 5.3 is done in analogy with the discretization of (48).

7.2 Modifications

The discretization of a $G_n^{(\text{ns})}$ becomes more difficult as n grows. The domain where the known asymptotics of its kernel is useful becomes narrower and forward recursion for $\mathfrak{Q}_{n-\frac{1}{2}}(\chi)$ becomes increasingly unstable. In previous work we let each quadrature panel along γ be temporarily divided into at most four subpanels for the resolution of $\mathfrak{Q}_{n-\frac{1}{2}}(\chi)$ at arguments close to unity and we used (expensive but stable) backward recursion whenever $\chi > 1.0005$. Here we allow up to six subpanels and use backward recursion, as in [9], whenever $\chi > 1.0001$.

Eigenwavenumbers are found with Broyden's method: Let $\lambda(k)$ be the smallest magnitude eigenvalue of the system matrix in (48) at wavenumber k . We seek eigenwavenumbers k as solutions to the system

$$\begin{aligned} \Re\{\lambda(k)\} &= 0, \\ \Im\{\lambda(k)\} &= 0, \end{aligned} \quad (72)$$

where $\Re\{k\}$ and $\Im\{k\}$ are considered independent unknowns. For an initial guess k that is reasonably close to a zero of $\lambda(k)$, Broyden's method converges to almost full achievable precision in about ten iterations.

WGMs with high indices n have eigendensities σ_n with numerically discernible support only on those parts of γ that lie farthest away from the z -axis. We exploit this property to reduce the number of unknowns when discretizing (48) in the search for high-index WGMs.

8 Numerical examples

Our Fourier–Nyström scheme for (48) and (44)–(47) is implemented in MATLAB and executed on a workstation equipped with an Intel Core i7-3930K CPU and 64 GB of memory. The implementation is standard and relies on built-in functions.

The examples we are about to present share some common features:

- The dielectric object is either the unit sphere or the object in Figure 1 whose generating curve γ has the parameterization

$$r(s) = (1 + 0.25 \cos(5s))(\sin(s), \cos(s)), \quad 0 \leq s \leq \pi. \quad (73)$$

- The refractive index is either $m = 1.5$ or $m = 1.5 + 5.5 \cdot 10^{-12}i$.
- The planar field plots show the absolute values of some of the coefficients $(H_{\rho n}(r), H_{\theta n}(r), H_{zn}(r))$ and $(E_{\rho n}(r), E_{\theta n}(r), E_{zn}(r))$. In each example, all six coefficients are evaluated and scaled with a common factor so that the largest pointwise value of at least one coefficient is unity. The coefficients are evaluated at $5 \cdot 10^5$ points r on a Cartesian grid in a rectangle of height 2.6 and width 1.3 and with its left side coinciding with the z -axis in the half-plane depicted in Figure 1(c). For ease of interpretation, we also show mirror images so that a field plot includes 10^6 points in a square of side length 2.6 in the xz -plane.
- The estimated errors in the field plots are taken as the absolute value of the pointwise difference to a reference solution. In the absence of semi-analytic solutions, the reference solution is obtained with an overresolved mesh containing 50 per cent more quadrature panels on γ . The error plots use a logarithmic scale.

Our examples cover two modal cases, both with high k : fundamental modes with large n and a general resonance with a small n . In addition to finding eigenwavenumbers and showing field plots we also do a convergence study, compute Q-values, and present far-field patterns.

8.1 The fundamental mode for large n

8.1.1 The unit sphere

Our first example is the fundamental $n = 90$ mode of the unit sphere with $m = 1.5$ and is intended as a verification of the solver. The reference solution is evaluated from a semi-analytic solution given by Mie theory [25]. The eigenwavenumber $k = 65.09451518155629 - 1.3 \cdot 10^{-13}i$, found by the solver, corresponds to a sphere diameter of 20.7 vacuum wavelengths and agrees with the value $k = 65.09451518155630 - 1.3 \cdot 10^{-13}i$, obtained from the semi-analytic solution, to almost machine precision.

Figure 2 shows field plots of $(|H_{\rho 90}(r)|, |H_{\theta 90}(r)|, |H_{z 90}(r)|)$ along with estimated absolute pointwise errors, which peak at around $100\epsilon_{\text{mach}}$. In passing we mention that our numerical tests revealed the following relations for the fundamental modes of dielectric spheres:

$$E_{\theta n}(r) = iE_{\rho n}(r) = i\frac{z}{\rho}E_{zn}(r), \quad (74)$$

which we then also derived from the semi-analytic solution.

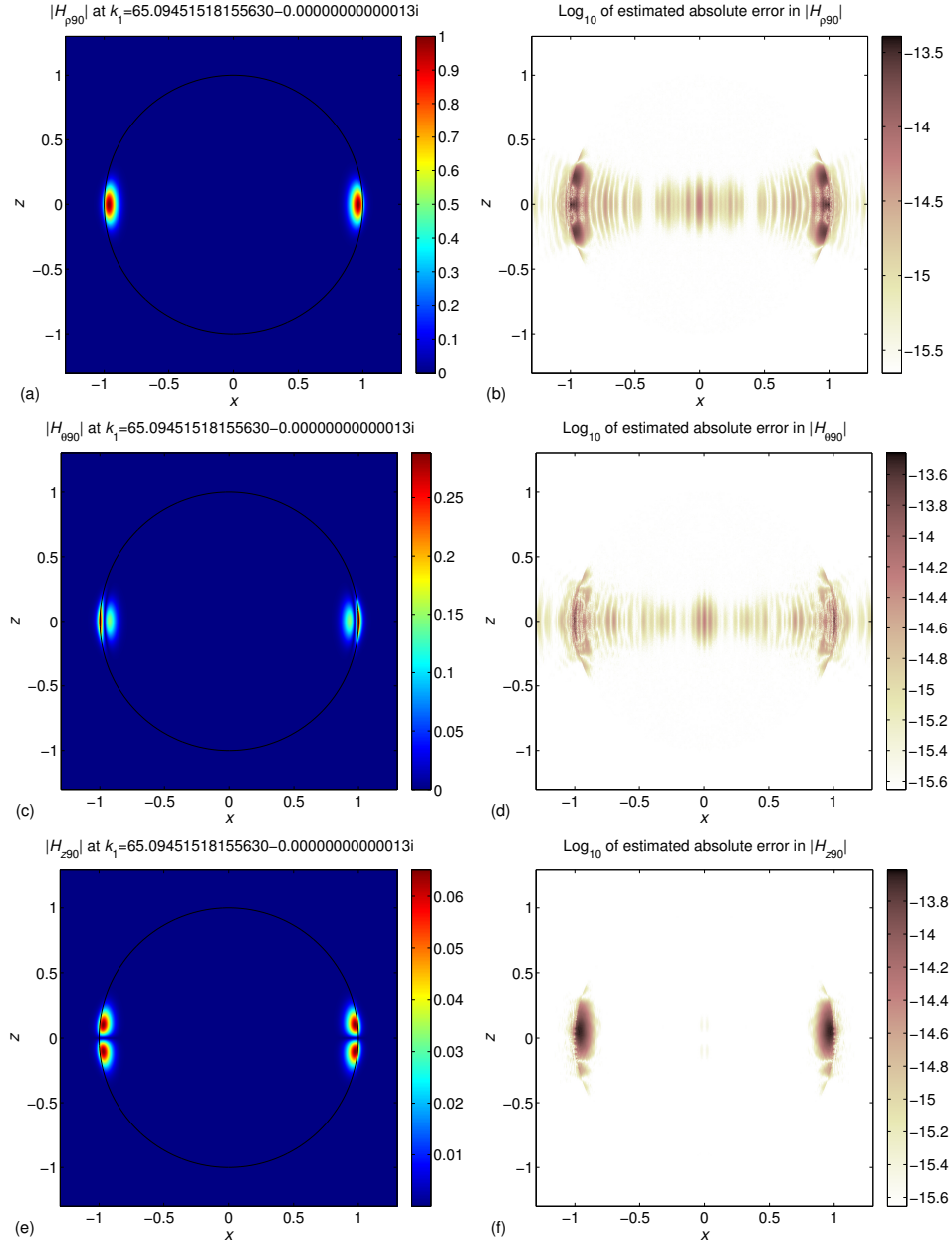


Figure 2: Planar field plots of the magnetic field for the fundamental $n = 90$ mode of a unit sphere with refractive index $m = 1.5$. The eigenwavenumber is $k = 65.09451518155630 - 1.3 \cdot 10^{-13}i$ and 832 discretization points are used on γ : (a), (c), and (e) show $|H_{\rho 90}(r)|$, $|H_{\theta 90}(r)|$, and $|H_{z 90}(r)|$; (b), (d), and (f) show \log_{10} of the estimated pointwise absolute error.

8.1.2 Lossless versus lossy object materials

We now look at the fundamental $n = 90$ mode of the object in Figure 1 and compare converged eigenwavenumbers and eigenfields for two different object materials. The first material is lossless with $m = 1.5$. The eigenwavenumber is $k = 54.72590089140112 - 1.5 \cdot 10^{-13}i$, corresponding to a generalized object diameter of about 22.8 vacuum wavelengths. The Q-factor (57) is $Q = 1.8 \cdot 10^{14}$. The second material is lossy with $m = 1.5 + 5.5 \cdot 10^{-12}i$ and has $k = 54.72590089140110 - 1.9803 \cdot 10^{-10}i$, which corresponds to a skin depth $\delta \approx 10^{10}$. The condition (65) is fulfilled and by that Q_{rad} is independent of $\Im\{m\}$ and (66) holds. A comparison of the eigenwavenumbers reveals that $\Re\{k\}$ is virtually unaffected by the losses. Since $Q_{\text{rad}} \gg Q_{\text{diss}}$, it follows from (60), (57), and (66) that $\Im\{k\}/\Re\{k\} \approx -\Im\{m\}/\Re\{m\}$. Now $Q = 1.382 \cdot 10^{11}$ and, since the lossless material has $Q = 1.8 \cdot 10^{14}$, the dissipative Q-factor is $Q_{\text{diss}} = 1.383 \cdot 10^{11}$ according to (60). This value agrees well with the approximate expression $Q_{\text{diss}} \approx 1.364 \cdot 10^{11}$ from (66).

The losses of the second material is the same as that of silica at the vacuum wavelength of 1550 nm, which is the smallest known loss of any solid material at optical wavelengths. It indicates that the physical limit for the Q-factor is approximately 10^{11} . To the eye, the field plots and the corresponding error plots with the lossless material and with the lossy material are indistinguishable. The images shown in Figure 3 are thus valid for both object materials.

8.1.3 A high wavenumber WGM

Figure 4 shows planar plots and error estimates of the magnetic field for the fundamental $n = 450$ mode of the object in Figure 1 with $m = 1.5$. The eigenwavenumber of this WGM is $k = 258.059066513439$, corresponding to a generalized object diameter of about 107.6 vacuum wavelengths. The imaginary part of k is not identically zero, but it is too small to be resolved in double precision arithmetic. The images in Figure 4 resemble those of the fundamental $n = 90$ mode in Figure 3, but with the fields confined to a smaller region and one digit of precision lost.

8.2 High k and small n

When $\Im\{m\} = 0$, resonances with high k and small n have much smaller Q-factors than fundamental modes with similar $\Re\{k\}$. We have clearly seen this in numerical test and it can also be understood from a phenomenological description of WGMs in terms of internal reflections. The eigenfields with high k and small n vary rapidly both outside and, in particular, inside A and the problem is harder to resolve.

Figures 5 and 6 show an example for the object in Figure 1 with $n = 1$ and $m = 1.5$. The converged eigenwavenumber $k = 110.041232211051 -$

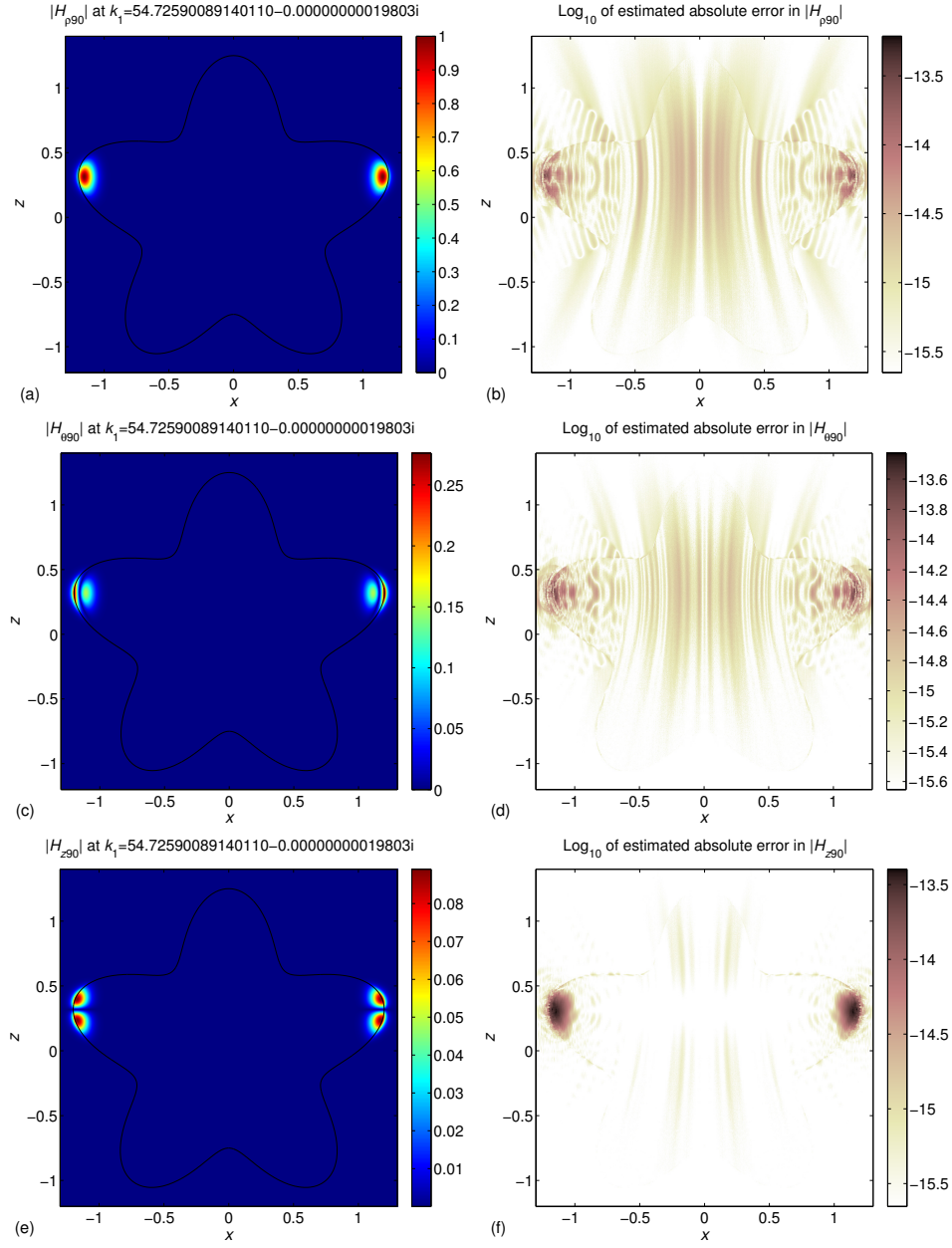


Figure 3: Same as in Figure 2, but for the object in Figure 1 and with $m = 1.5 + 5.5 \cdot 10^{-12}i$. The eigenwavenumber is $k = 54.72590089140110 - 1.9803 \cdot 10^{-10}i$ and 864 discretization points are used on γ .

$0.404177078290i$ corresponds to a generalized object diameter of about 45.9 vacuum wavelengths. The large value of $\Im\{k\}$ makes the exponential growth of the eigenfields visible already in the object's immediate vicinity.

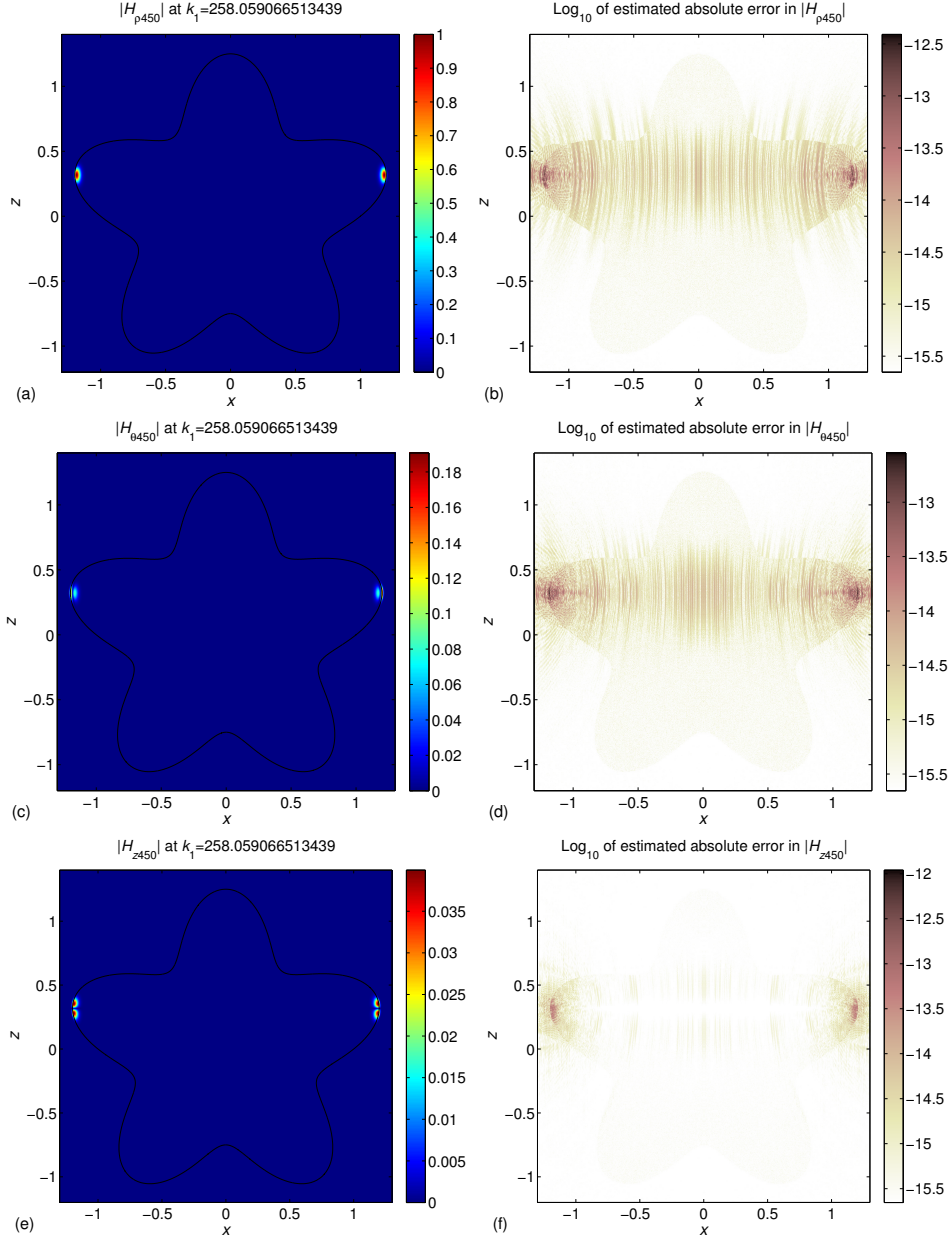


Figure 4: Same as in Figure 3, but for $n = 450$ and with $m = 1.5$. The eigenwavenumber is $k = 258.059066513439$ and 352 adaptively spaced discretization points are used on γ .

Figure 7 confirms that our solver exhibits 16th order convergence and is stable under uniform overresolution. The average pointwise accuracy in the field plots saturates at 12–13 digits, which compares favorably with the most accurate results we have found in the literature for general transmission

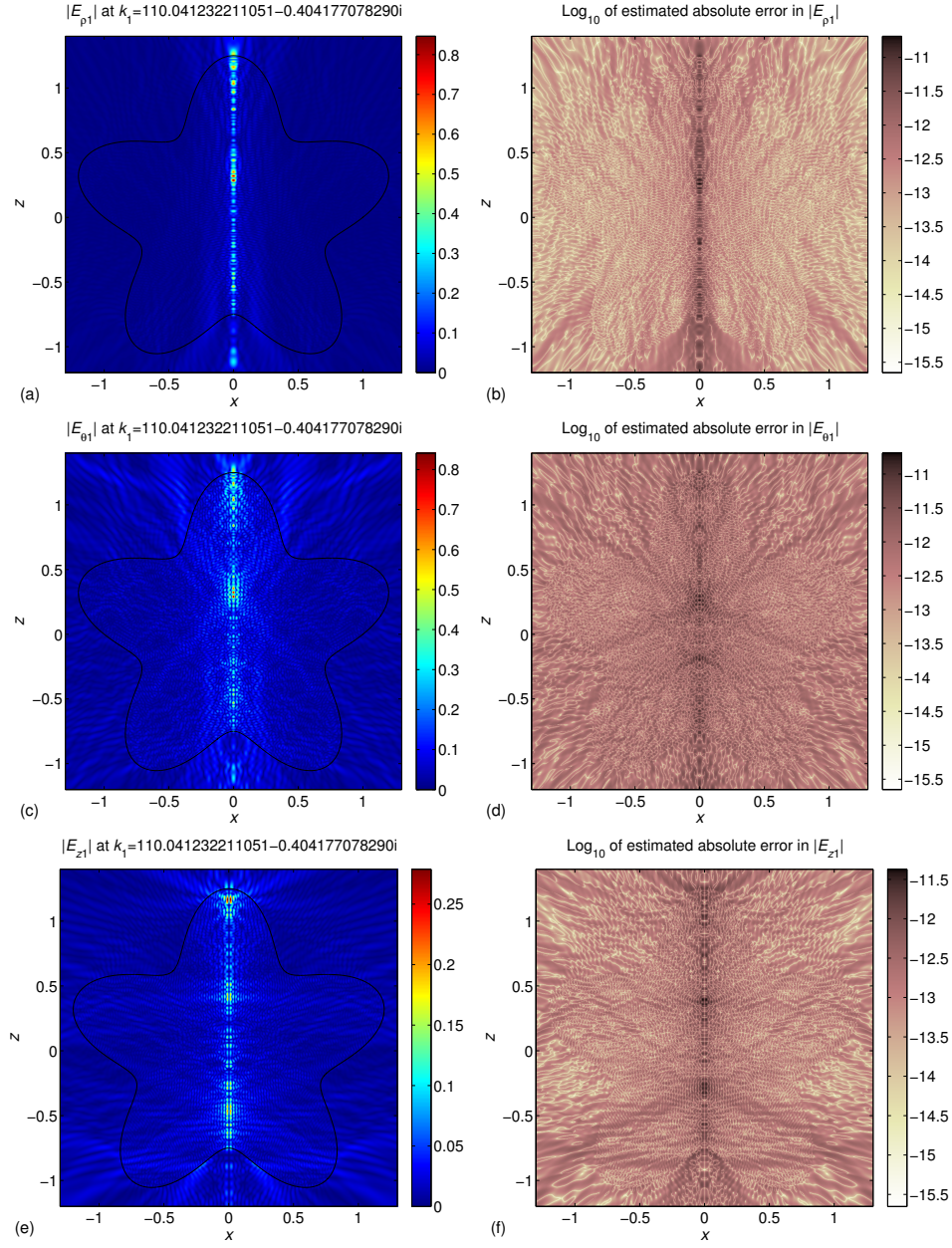


Figure 5: Planar field plots of the electric field for an $n = 1$ mode of the object in Figure 1. The eigenwavenumber is $k = 110.041232211051 - 0.404177078290i$, the refractive index is $m = 1.5$, and 1984 discretization points are used on γ .

problems involving axially symmetric objects of non-trivial shapes [20].

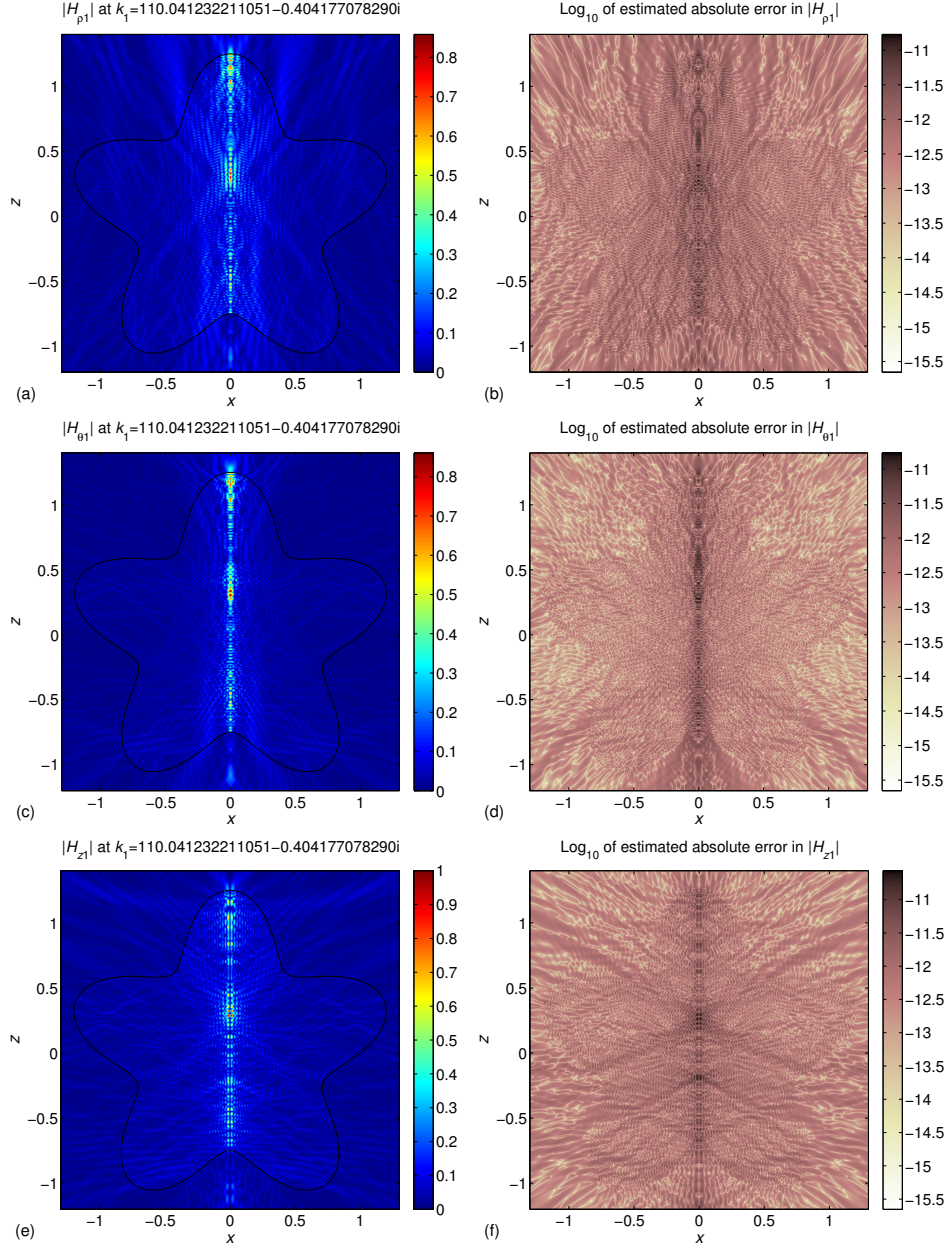


Figure 6: Same as in Figure 5, but for the magnetic field.

8.3 Far-field patterns

Far-field patterns of resonant modes are defined by (67) and (68). A necessary condition for their meaningful evaluation when $\Im m\{m\} = 0$ is that $\Im m\{k\}$ is known with a relative accuracy better than one per cent. This means that if Q_{rad} , which for $\Im m\{m\} = 0$ is equal to Q , is on the order of

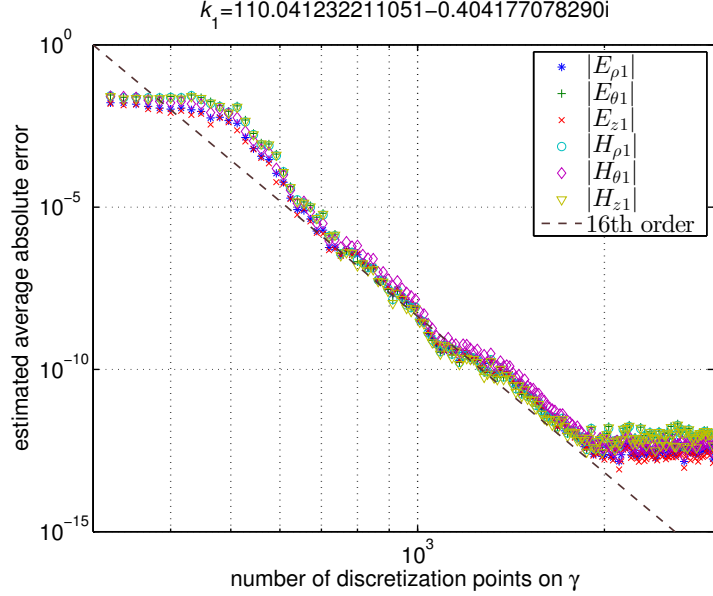


Figure 7: Convergence of the field plots shown in Figures 5 and 6. The average pointwise accuracy has converged to between 12 and 13 digits at 1900 discretization points on γ , corresponding to about 26 points per vacuum wavelength along γ .

10^p , then k needs to be resolved with at least $p + 2$ digits. This condition, coupling the magnitude of Q_{rad} to the precision required in k , seems to hold also when $\Im m\{m\} \neq 0$. The requirement of $p + 2$ accurate digits in k is met in all our examples, except for that of the high wavenumber WGM in Section 8.1.3.

Figure 8 shows that the far-field patterns of the WGMs are smooth and resemble each other. Their radiated fields peak at the equator, $\phi = \pi/2$. The variation in the pattern of the $n = 1$ mode of Section 8.2 is rapid, as expected.

9 Conclusions

The construction of Fredholm second kind integral equation based solvers for electromagnetic transmission problems is an active and multifaceted research field [3, 8, 20]. Our solver, for the determination of resonant modes of axially symmetric dielectric objects, uses charge integral equations [26] within the classical Müller formulation [22]. This, in combination with a high-order convergent discretization [13], allows for exceptionally accurate results and excludes the possibility of finding spurious solutions. Moreover, the solver extends the admissible size of objects for which high accuracy

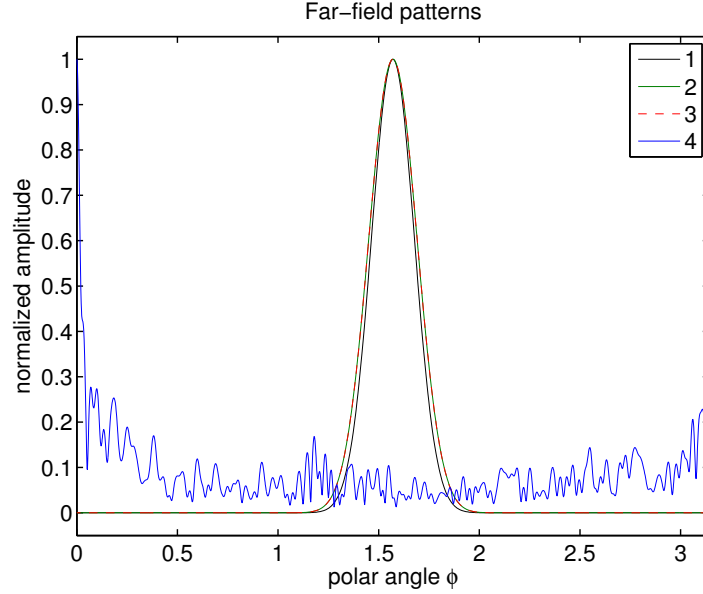


Figure 8: Far-field patterns: curve 1 is for the WGM of the unit sphere of Section 8.1.1; curves 2 and 3, which are almost identical, are for the WGMs with lossless and lossy object materials of Section 8.1.2; curve 4 is for the $n = 1$ mode of Section 8.2.

can be obtained, based on the full vectorial Maxwell equations, into the regime where asymptotic methods for WGMs are applicable [2] (diameters of around 200 vacuum wavelengths). We stress the following capabilities of our solver up to such object sizes:

- The evaluation of the entire spectrum and all eigenfields with $\Re\{k\}$ in a given interval. This includes the computationally difficult resonances with small n and high k .
- The evaluation of eigenfields at any point in space. This includes slowly-evanescent and radiated fields.
- The evaluation of far-field patterns of WGMs with radiative Q-factors up to 10^{13} .
- Geometric flexibility. While high-order surface information is a prerequisite, non-smooth boundaries can be treated using techniques from [15].

These capabilities open up for new studies related to the coupling of light into WGMs, to finding new object shapes for WGMs and resonances in objects with non-linear materials and materials with optical gain. They also make the solver ideal for benchmarking.

Acknowledgement

This work was supported by the Swedish Research Council under contract 621-2014-5159.

Appendix A. The operators K_{24n} , K_{25n} , and K_{26n}

The modal operators K_{in} , $i = 24, 25, 26$, are most easily defined in terms of (36) and (37) and the kernels

$$K_i(\mathbf{r}, \mathbf{r}') = D_i(\mathbf{r}, \mathbf{r}')(1 - ik|\mathbf{r} - \mathbf{r}'|)e^{ik|\mathbf{r} - \mathbf{r}'|}, \quad i = 24, 25, 26, \quad (\text{A.1})$$

with static factors

$$D_{24}(\mathbf{r}, \mathbf{r}') = \frac{\boldsymbol{\tau} \cdot (\mathbf{r} - \mathbf{r}')}{4\pi|\mathbf{r} - \mathbf{r}'|^3}, \quad (\text{A.2})$$

$$D_{25}(\mathbf{r}, \mathbf{r}') = i \frac{(\nu_\rho \nu' \cdot \mathbf{r}' + \nu'_z \boldsymbol{\tau} \cdot \mathbf{r}) \sin(\theta - \theta')}{4\pi|\mathbf{r} - \mathbf{r}'|^3}, \quad (\text{A.3})$$

$$D_{26}(\mathbf{r}, \mathbf{r}') = \frac{\nu_z \rho' - (\boldsymbol{\tau} \cdot \mathbf{r} + \nu_\rho z') \cos(\theta - \theta')}{4\pi|\mathbf{r} - \mathbf{r}'|^3}. \quad (\text{A.4})$$

and, with notation as in [15, Appendix A], corresponding Fourier coefficients

$$D_{24n}(r, r') = -\eta \left[d(\tau) \Re_n(\chi) - \frac{\nu_z}{\rho} \Im_n(\chi) \right], \quad (\text{A.5})$$

$$D_{25n}(r, r') = \eta \frac{(\nu_\rho \nu' \cdot \mathbf{r}' + \nu'_z \boldsymbol{\tau} \cdot \mathbf{r})}{\rho \rho'} n \Im_{n-\frac{1}{2}}(\chi), \quad (\text{A.6})$$

$$D_{26n}(r, r') = \eta \left[d(\tau) \Re_n(\chi) + \frac{(\boldsymbol{\tau} \cdot \mathbf{r} + \nu_\rho z')}{\rho \rho'} \Im_n(\chi) \right]. \quad (\text{A.7})$$

The reason for including (A.5)-(A.7) in this exposition is that these expressions are used in the convolutions in our numerical scheme, see Section 7.1.

References

- [1] V. Amendola, O.M. Bakr, and F. Stellacci, “A study of the surface plasmon resonance of silver nanoparticles by the discrete dipole approximation method: effect of shape, size, structure, and assembly,” *Plasmonics* **5**, 85–97 (2010).
- [2] I. Breunig, B. Sturman, F. Sedlmeir, H.G.L. Schwefel, and K. Buse, “Whispering gallery modes at the rim of an axisymmetric optical resonator: Analytical versus numerical description and comparison with experiment,” *Opt. Express* **21**, 30683–30692 (2013).
- [3] V.S. Bulygin, Y.V. Gandel, A. Vukovic, T.M. Benson, P. Sewell, and A.I. Nosich, “Nystrom method for the Muller boundary integral equations on a dielectric body of revolution: axially symmetric problem,” *IET Microw. Antennas Propag.* **9**, 1186–1192 (2015).

- [4] Y.K. Chembo and N. Yu, “Modal expansion approach to optical-frequency-comb generation with monolithic whispering-gallery-mode resonators,” *Phys. Rev. A* **82**, 033801 (2010).
- [5] H.S. Cohl and J.E. Tohline, “A compact cylindrical Green’s function expansion for the solution of potential problems,” *Astrophys. J.* **527**, 86–101 (1999).
- [6] D. Colton and R. Kress, *Inverse acoustic and electromagnetic scattering theory*, (Springer, 2013), 3rd ed.
- [7] M.R. Foreman, J.D. Swaim, and F. Vollmer, “Whispering gallery mode sensors,” *Adv. Opt. Photon.* **7**, 168–240 (2015).
- [8] M. Ganesh, S.C. Hawkins, and D. Volkov, “An all-frequency weakly-singular surface integral equation for electromagnetism in dielectric media: Reformulation and well-posedness analysis,” *J. Math. Anal. Appl.* **412**, 277–300 (2014).
- [9] A. Gil, J. Segura, and N.M. Temme, *Numerical Methods for Special Functions*, (SIAM, 2007), Remark 3, p. 106.
- [10] I.S. Gradshteyn and I.M. Ryzhik, *Table of Integrals, Series, and Products*, (Elsevier, 2007), 7th ed., Eq. 8.713.1.
- [11] L. He, Ş.K. Özdemir, and L. Yang, “Whispering gallery microcavity lasers,” *Laser Photon. Rev.* **7**, 60–82 (2013).
- [12] J. Helsing and A. Holst, “Variants of an explicit kernel-split panel-based Nyström discretization scheme for Helmholtz boundary value problems,” *Adv. Comput. Math.* **41**, 691–708 (2015).
- [13] J. Helsing and A. Karlsson, “An explicit kernel-split panel-based Nyström scheme for integral equations on axially symmetric surfaces,” *J. Comput. Phys.* **272**, 686–703 (2014).
- [14] J. Helsing and A. Karlsson, “Determination of normalized magnetic eigenfields in microwave cavities,” *IEEE Trans. Microw. Theory Tech.* **63**, 1457–1467 (2015).
- [15] J. Helsing and A. Karlsson, “Determination of normalized electric eigenfields in microwave cavities with sharp edges,” *J. Comput. Phys.* **304**, 465–486 (2016).
- [16] E. Heyman and L. Felsen, “Creeping waves and resonances in transient scattering by smooth convex objects,” *IEEE Trans. Antennas Propag.* **31**, 426–437 (1983).
- [17] J.D. Jackson, *Classical electrodynamics*, (Wiley, 1999), 3rd ed.
- [18] T.J. Kippenberg, R. Holzwarth, and S.A. Diddams, “Microresonator-based optical frequency combs,” *Science* **332**, 555–559 (2011).
- [19] A.A. Kishk, Y. Yin, and A.W. Glisson, “Conical dielectric resonator antennas for wide-band applications,” *IEEE Trans. Antennas Propag.* **50**, 469–474 (2002).
- [20] Y. Liu and A.H. Barnett, “Efficient numerical solution of acoustic scattering from doubly-periodic arrays of axisymmetric objects,” arXiv:1506.05083 [math.NA]

- [21] A.B. Matsko and V.S. Ilchenko, “Optical resonators with whispering gallery modes I: basics,” *IEEE J. Sel. Top. Quantum Electron.* **12**, 3–14 (2006).
- [22] C. Müller, *Foundations of the Mathematical Theory of Electromagnetic Waves*, (Springer, 1969).
- [23] M. Oxborrow, “Traceable 2-D finite-element simulation of the whispering-gallery modes of axisymmetric electromagnetic resonators,” *IEEE Trans. Microw. Theory Tech.* **55**, 1209–1218 (2007).
- [24] I.M. Reaney and D. Iddles, “Microwave dielectric ceramics for resonators and filters in mobile phone networks,” *J. Am. Ceram. Soc.* **89**, 2063–2072 (2006).
- [25] J.A. Stratton, *Electromagnetic Theory*, (McGraw-Hill, 1941), p. 615.
- [26] M. Taskinen and P. Ylä-Oijala, “Current and charge integral equation formulation,” *IEEE Trans. Antennas Propag.* **54**, 58–67 (2006).
- [27] F. Vico, Z. Gimbutas, L. Greengard, and M. Ferrando-Bataller, “Overcoming low-frequency breakdown of the magnetic field integral equation,” *IEEE Trans. Antennas Propag.* **61**, 1285–1290 (2013).
- [28] J. Wiersig, “Boundary element method for resonances in dielectric microcavities,” *J. Opt. A: Pure Appl. Opt.* **5**, 53–60 (2003).
- [29] P. Ylä-Oijala and M. Taskinen, “Well-conditioned Müller formulation for electromagnetic scattering by dielectric objects,” *IEEE Trans. Antennas Propag.* **53**, 3316–3323 (2005).
- [30] P. Young, S. Hao, and P.G. Martinsson, “A high-order Nyström discretization scheme for boundary integral equations defined on rotationally symmetric surfaces,” *J. Comput. Phys.* **231**, 4142–4159 (2012).
- [31] W. Zheng and S. Ström, “The null-field approach to electromagnetic resonance of composite objects,” *Comput. Phys. Commun.* **68**, 157–174 (1991).